Journal of Energy Storage 108 (2025) 115044

Contents lists available at ScienceDirect

Journal of Energy Storage

journal homepage: www.elsevier.com/locate/est

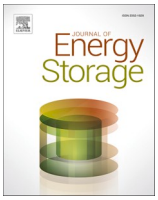

Research Papers

Battery state prediction through hybrid modeling: Integrating neural networks with a single particle model

Simona Pepe [a,1], Lok Shu Kwan [a,1], Baptiste Py [a,2], Matthew J. Robson [a,2], Adeleke Maradesa [a], Francesco Ciucci [b,c,*]

[a] Department of Mechanical and Aerospace Engineering, The Hong Kong University of Science and Technology, Hong Kong
[b] Chair of Electrode Design for Electrochemical Energy Systems, University of Bayreuth, 95448 Bayreuth, Germany
[c] University of Bayreuth, Bavarian Center for Battery Technology (BayBatt), Universitätsstraße 30, 95447 Bayreuth, Germany

ARTICLE INFO

Keywords:
Single particle model
Machine learning
Battery aging
Battery management system
Lithium-ion batteries

ABSTRACT

Battery energy storage systems are vital for a variety of applications, with a particularly important role in facilitating the widespread use of renewable energy resources and electric vehicles. To ensure the safety and optimal performance of these devices, analyzing their operation through physical and data-driven models is essential. While physical models can effectively model the underlying physicochemical processes, their complexity often renders them impractical for real-time onboard diagnostics. Conversely, data-driven models are usually more flexible and easier to implement, but they lack a physical description of the battery. In response to these challenges, this work models the battery state using a single particle model as a baseline for subsequent predictions made with neural networks. To achieve this, two neural networks were leveraged: one to apply a correction to the voltage obtained from the physical model, and the second to evaluate the battery state of health and aging states. The novel hybrid model, integrating a single particle model with two neural networks, consistently outperformed both the individual single particle model and the two neural networks in isolations. Results were benchmarked using two real-world battery cycling datasets, including one collected in-house. The hybrid model consistently outperformed the individual neural networks in terms of voltage prediction accuracy, as evidenced by lower root mean square error (RMSE) values. Notably, in four out of the five cases where the analysis was stratified by battery manufacturer, the RMSE was reduced by at least 50 % and up to tenfold with the hybrid approach. Given the promise of this new hybrid model, it is expected that the present work will pave the way for advanced modeling of batteries.

1. Introduction

To combat climate change, humanity needs to transition to renewable energy sources [1]. Consequently, batteries, which can store and discharge energy from renewable sources on demand [2], have become increasingly central to modern life [3]. Battery management systems are critical to maximizing battery performance, safety, and lifetime; monitoring currents and voltages in real-time can prevent battery overcharging [4], over-discharging, and thermal runaway [5]. Battery management systems typically use equivalent circuits or physical models to analyze the battery response to input currents. Although the latter can be more accurate given their physics-based framework, they require accurate knowledge of the physicochemical mechanisms underlying battery operation and operating conditions. Moreover, battery parameters (*e.g.,* areal mass loading of active material in the cathode (mg/cm^2) or electrolyte conductivity [6,7]) are often not readily available [8]. This reduces the generalizability and applicability of physical models. Additionally, the application of physical models, such as the Doyle-Fuller-Newman model [6], has been limited in battery management systems due to the high computational demand for onboard predictions [8]. To reduce the computational effort, simplified models [8,9], such as single particle models (SPMs) [10], have been proposed. However, SPMs treat all particles within a battery electrode as exhibiting identical behavior, limiting their accuracy under intermittent

* Corresponding author at: Chair of Electrode Design for Electrochemical Energy Systems, University of Bayreuth, 95448 Bayreuth, Germany.
E-mail address: francesco.ciucci@uni-bayreuth.de (F. Ciucci).
[1] Equally contributing authors.
[2] Equally contributing authors.

https://doi.org/10.1016/j.est.2024.115044
Received 21 November 2023; Received in revised form 30 September 2024; Accepted 11 December 2024
Available online 24 December 2024

currents and extreme temperatures [11].

To overcome these limitations, several machine learning (ML) models have been developed [12]. Notably, ML models demonstrate superior flexibility and generalizability over physical models due to their ability to identify complex patterns within large datasets. Such models have been shown to perform better than physical models with respect to battery life prediction [13] and cycling protocol development [14,15]. Additionally, ML models do not require *a priori* knowledge regarding the underlying physicochemical processes, instead relying only on performance data [16]. Nonetheless, achieving high accuracy with ML models usually involves training on large datasets, which are not always available.

Leveraging the advantages of physical and ML models, hybrid models, which combine both techniques, can accurately learn current-voltage dependencies [17,18]. Such hybrid models combine physics-based understanding of the battery with the flexibility and adaptability of ML models. Combining these models, therefore, enables a more comprehensive and generalizable prediction of battery performance and lifetime. While only a few works have focused on hybrid models for battery modeling [17,19,20], aging models have yet to be included in hybrid models. To the authors' knowledge, only Tu et al. [18] have demonstrated the advantages of introducing the state of health (SOH) as a parameter to establish battery degradation.

We propose a novel hybrid model (ML + SPM) combining an SPM with two neural networks to simultaneously parametrize the battery SOH and current-voltage responses. Specifically, we used a neural network based on ordinary differential equations (neural-ODE) [21] and a long-short-term memory (LSTM) recurrent neural network [22]. Given that neural-ODEs are known for their accuracy and ability to predict SOH curves over a long lifespan range [23], we used a neural-ODE to recover the battery health parameters, including the SOH and total times for complete charge and discharge, which are all functions of the cycle number [21]. Moreover, we integrated the LSTM recurrent neural network due to its ability to 1) regress currents and voltages using feedback loop structure, and 2) accurately propagate the memory of the past history into future states [24]. In this work, an SPM model parameterized using available cell specifications and operating conditions was harnessed to provide the LSTM model with a baseline voltage profile during the discharge. Therefore, the LSTM was used to correct the regressed voltage, accounting for missing physical knowledge and aging profile shifts. In addition to the ML + SPM model, two neural networks were studied without the SPM correction (ML model), where the LSTM was used to directly compute the voltages from aging parameters and input currents after each discharging cycle. The ML and ML + SPM models were benchmarked using two datasets, including one generated by our group (denoted as 'HKUST dataset'), and the Oxford dataset [25,26]. Both datasets are representative of real-life applications where limited knowledge about battery properties is available.

Our results highlight the strengths and limitations of ML and ML + SPM models for battery analysis. The hybrid ML + SPM model significantly improves performance in key areas. When analyzing batteries subjected to diverse cycling protocols, the integrated SPM boosts the model's accuracy in predicting current-voltage responses by providing a physical baseline. The neural-ODE accurately models battery degradation within the LSTM, allowing us to predict time-dependent voltage profiles and to inform battery health evolution. Our ML + SPM model outperformed the standalone ML model in most cases, demonstrating superior voltage prediction accuracy. This novel approach, combining an SPM with two neural networks, simultaneously calculates battery SOH and current-voltage responses. In short, by directly incorporating aging information, our model delivers more accurate predictions and streamlines battery analysis.

2. Cycling data

2.1. HKUST battery dataset

To assess the quality of our approach against experimental data, a new battery cycling dataset was collected in-house. To obtain this data, batteries were tested from five different manufacturers, namely CHAM, EVE, LISHEN, MOLICEL and SAMSUNG, all of which are identified by the same names. Six cells of each type were purchased from the manufacturers, and the cathode type, external dimensions, and nominal capacity of each cell are reported in Table 1. All cells tested were cylindrical-type 21700 cells, except for the 18650-type EVE batteries. The CHAM and LISHEN cells were constructed with $LiNi_xMn_yCo_{1-x-y}O_2$ (NMC) cathodes with an unspecified stoichiometry, while the EVE and MOLICEL cells used $LiNi_{0.8}Mn_{0.1}Co_{0.1}O_2$ (NMC811) cathodes. Lastly, the SAMSUNG cells used a nickel cobalt aluminum (NCA) cathode. The batteries were cycled using a Neware BTS-4008T 5V6A-S1 battery cycle tester at room temperature ($25^{\circ}C \pm 2^{\circ}C$) according to heavy or light charge-discharge profiles (see Table 1). For the heavy charge-discharge profile, the batteries were charged using a constant-current constant-voltage (CC-CV) charging protocol, comprising an initial CC charge step to 4.2V at 0.5C followed by a CV step that held the batteries at 4.2V until a current of 0.02C was reached. The cells were then discharged at 1C until the voltage reached 2.5 V. For the light cycling profile, a similar CC-CV charge protocol was used, this time with an initial CC charge to 4.1 V at 0.5C, then CV charging at 4.1 V until the current decayed to 0.02C. Constant current discharge at 1C was then performed with a lower voltage cutoff of 3.0 V. In all cases, the batteries were rested for 10 min between the charge and discharge. The C-rate for each cell was calculated using the manufacturer-specified nominal capacity.

2.2. Oxford battery dataset

In addition to the HKUST dataset, eight commercial Kokam (SLPB533459H4) lithium-ion batteries cycled at Oxford University [26] were considered. These cells, which are characterized by a 740-mAh nominal capacity, were repeatedly discharged using the dynamic Artemis urban drive cycle and recharged at a constant 2C rate. Every 100 cycles, a constant-current discharge with a rate of 1C was performed to characterize the battery discharge performance and SOH. The end of life of the batteries was observed after approximately 8000 cycles.

3. Methods

3.1. Models

3.1.1. Single particle model

The Python Battery Mathematical Modelling (PyBAMM) package (version 22.3) [7] was used to generate first-cycle discharge-voltage profiles for each of the tested batteries using an included SPM that describes the voltage, V, as [27]

$$V = U_p - U_n - \frac{2RT}{F}\left(sinh^{-1}\left(\frac{I}{2j_{0,p}a_pL_p}\right) + sinh^{-1}\left(\frac{I}{2j_{0,n}a_pL_n}\right)\right) \quad (1)$$

where U_p and U_n are the open circuit potentials of the positive, p, and negative, n, electrode, respectively, R is the universal gas constant, T is the temperature, F is the Faraday constant, I is the current, a_p and a_n are the surface area of the positive and negative electrodes, respectively, and L_p and L_n are the thickness of the positive and negative electrodes, respectively. Moreover, the exchange current densities $j_{0,p}$ and $j_{0,n}$ for the positive and negative electrodes, respectively, are defined as

$$j_{0,p} = \sqrt{c_p(1-c_p)} \quad (2a)$$

Table 1
Characteristics of the cycling experiments in the HKUST dataset.

Manufacturer	EVE	CHAM	LISHEN	MOLICEL	SAMSUNG
Cathode	NMC-811	NMC	NMC	NMC-811	NCA
Battery type	18650	21700	21700	21700	21700
Nominal capacity (Ah)	2.8	5.0	4.0	4.2	4.9
Heavy charging protocol	Constant current 0.5 C (1.4 A), constant voltage (4.2 V), and cut-off current 0.02 C (0.056 A)	Constant current 0.5 C (2.5 A), constant voltage (4.2 V), and cut-off current 0.02 C (0.01 A)	Constant current 0.5 C (2.0 A), constant voltage (4.2 V), and cut-off current 0.02 C (0.08 A)	Constant current 0.5 C (2.1 A), constant voltage (4.2 V), and cut-off current 0.02 C (0.084 A)	Constant current 0.5 C (2.45 A), constant voltage (4.2 V), and cut-off current 0.02 C (0.097 A)
Light charging protocol	Constant current 0.5 C (1.4 A), constant voltage (4.1 V), and cut-off current 0.02 C (0.056 A)	Constant current 0.5 C (2.5 A), constant voltage (4.1 V), and cut-off current 0.02 C (0.01 A)	Constant current 0.5 C (2.0 A), constant voltage (4.1 V), and cut-off current 0.02 C (0.08 A)	Constant current 0.5 C (2.1 A), constant voltage (4.1 V), and cut-off current 0.02 C (0.084 A)	Constant current 0.5 C (2.45 A), constant voltage (4.2 V), and cut-off current 0.02 C (0.097 A)
Heavy discharging protocol	Constant current 1 C (2.8 A), cut-off voltage (2.5 V)	Constant current 1 C (5.0 A), cut-off voltage (2.5 V)	Constant current 1 C (4.0 A), cut-off voltage (2.5 V)	Constant current 1 C (4.2 A), cut-off voltage (2.5 V)	Constant current 1 C (4.9 A), cut-off voltage (2.5 V)
Light discharging protocol	Constant current 1 C (2.8 A), cut-off voltage (3.0 V)	Constant current 1 C (5.0 A), cut-off voltage (3.0 V)	Constant current 1 C (4.0 A), cut-off voltage (3.0 V)	Constant current 1 C (4.2 A), cut-off voltage (3.0 V)	Constant current 1 C (4.9 A), cut-off voltage (3.0 V)
Cycle sequence	Rest–charge–rest–discharge	Rest–charge–rest–discharge	Rest–charge–rest–discharge	Rest–charge–rest–discharge	Rest–charge–rest–discharge

$$j_{0,n} = \sqrt{c_n(1-c_n)} \tag{2b}$$

where c_p and c_n are the lithium concentration at the positive and negative electrode, respectively. More details about this SPM can be found in the literature [27].

For the HKUST dataset, batteries with NMC cathodes and NCA cathodes were modeled using the Chen2020 [28] and NCA_Kim2011 [29] as base parameter sets, respectively. The physical and chemical parameters of the HKUST batteries were matched to manufacturer data (where available), and the PyBAMM experimental parameters were subsequently set to replicate the real-world cycling protocol used for the HKUST batteries (more details are given in Table 1). Furthermore, the Ecker2015 parameter set included in PyBAMM was used as a baseline to model a Kokam SLPB533459H4 pouch cell and generate representative discharge voltage profiles for the Oxford dataset [30–34]. The manufacturer specifications for the Oxford batteries were then used to define the electrode's dimensions, cell cooling surface area, cell volume, and nominal cell capacity. The PyBAMM experimental parameters were set by matching the initial temperature, ambient temperature, current function, and upper and lower voltage cut-offs to the testing protocol from the Oxford dataset. Voltage curves were then simulated for the first discharge cycle using the SPM. The values of the parameters used are reported in Table S1 of the Supplementary Information (SI).

3.1.2. Machine learning model

The architecture for the ML model is combined with the neural-ODE and LSTM (see Section 1) to obtain time-dependent voltage profiles from aging parameters (more details are given in Section 3.2) and input currents, respectively. Neural-ODEs, as originally proposed by Chen [35], are deep neural networks designed to model the evolution over time of the states, $\boldsymbol{y}$, of a system. These states follow this relation [23]:

$$\dot{\boldsymbol{y}} = F(t, \boldsymbol{y}) \tag{3}$$

where the function $F(\bullet)$ is assumed to be autonomous and parameterized through an infinitely deep neural network. The dynamics of the neural-ODE can be reformulated as a continuous ODE problem within an infinitesimal time step. An ODE solver then computationally determines system states, starting from an initial value, while simultaneously learning the function $F(\bullet)$. Earlier research demonstrates the strong performance of ODE-based models in uncovering intrinsic dynamics and predicting outcomes for battery degradation parameters, including the SOH [23].

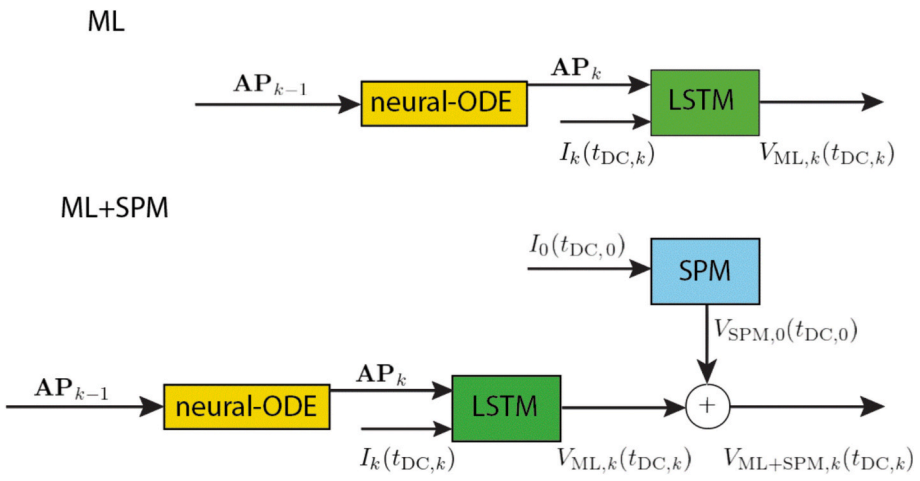

Fig. 1. The upper and lower panels show a schematic representation of the architecture of the ML and ML + SPM models, respectively. $\mathbf{AP}_k$, $I_k(t_{\mathrm{DC},k})$, $V_{\mathrm{ML},k}(t_{\mathrm{DC},k})$, and $V_{\mathrm{ML+SPM},k}(t_{\mathrm{DC},k})$ denote the vector of aging parameters, current, ML-based voltage, and ML + SPM-based voltage at the cycle k and over the time for the full discharge $t_{\mathrm{DC},k}$, respectively, while $V_{\mathrm{SPM},0}(t_{\mathrm{DC},0})$ is the SPM-based voltage at the initial cycle. We stress that the neural-ODE only uses $\mathbf{AP}_{k-1}$ to predict $\mathbf{AP}_k$.

Moreover, the architecture of the ML model is displayed in Fig. 1. The parameters for each neural network are given in Table S2.

3.1.3. Hybrid model

The architecture of the ML + SPM model, see Fig. 1, leverages an LSTM integrated with a neural-ODE and the SPM. To compute the voltage profiles, the LSTM was used to obtain a correction term ($V_{\mathrm{SPM},k}(t_k)$), which was subsequently applied to a baseline voltage curve generated by the SPM model [19]. The neural-ODE network was used to fit and predict the battery aging parameters, which were then fed to the LSTM to evaluate the current cycle and future states. Moreover, Fig. 2 provides a flowchart illustrating the complete structure of our new ML + SPM model, highlighting the key roles of the SPM and ML components.

The parameters for each neural network are given in Table S2.

3.2. Aging features

Since the SOH cannot be readily measured [36], the aging state of the cells was parametrized as a function of the cycle number using three quantities derived from the dataset. First, the SOH at the k-th cycle, SOH_k, was expressed as the ratio of the capacity at the k-th cycle, Q_k, divided by the total capacity of a fresh battery, Q_0, *i.e.*,

$$\mathrm{SOH}_k = \frac{Q_k}{Q_0} \tag{4}$$

Additionally, the k-th cycle (total) charge, $t_{\mathrm{C},k}$, and discharge, $t_{\mathrm{DC},k}$, times were considered at constant current because these two quantities have been identified as primary predictors of battery aging by Hu et al. [36]. Moreover, $t_{\mathrm{C},k}$ and $t_{\mathrm{DC},k}$ are expected to decrease with the battery lifetime due to the increase in battery internal resistance, mirroring the SOH. It is expected that the combination of $t_{\mathrm{C},k}$ and $t_{\mathrm{DC},k}$ will improve the SOH prediction since the SOH_k alone is not sufficiently informative of battery internal decay, especially early in the battery lifetime [37]. Next, the vector, $\mathbf{AP}_k$, of aging parameters was defined as

$$\mathbf{AP}_k = \begin{pmatrix} \mathrm{SOH}_k \\ t_{\mathrm{C},k} \\ t_{\mathrm{DC},k} \end{pmatrix} \tag{5}$$

where $\mathbf{AP}_k$ is the vector input of the neural-ODE network at the cycle k, see Fig. 1. We stress that the output of this neural network is the vector, $\mathbf{AP}_{k+1}$, of aging parameters at the following cycle. Moreover, the input vector to the LSTM at the k-th cycle includes $\mathbf{AP}_k$ from the neural-ODE, and the current imposed for a full discharge cycle, $I_k(\mathrm{t})$. Importantly, the latter was discretized with 100 collocation points over the discharging period. In the case of the HKUST dataset, three additional features were considered: one feature used to identify the manufacturer, each represented by a numerical value between 0 and 1, and two features identifying the upper and lower cut-off voltage values to distinguish heavy and light cycling protocols (Section 2.1).

3.2.1. Error metrics

Model performance was benchmarked with the voltage root-mean-square error (RMSE) for regression, $\mathrm{RMSE}_{\mathrm{reg}}$, which is defined as the following quantity:

$$\mathrm{RMSE}_{\mathrm{reg}} = \sqrt{\frac{1}{N_{\mathrm{reg}}} \sum_{k=1}^{N_{\mathrm{reg}}} (\widehat{V}_k - V_k)^2} \tag{6}$$

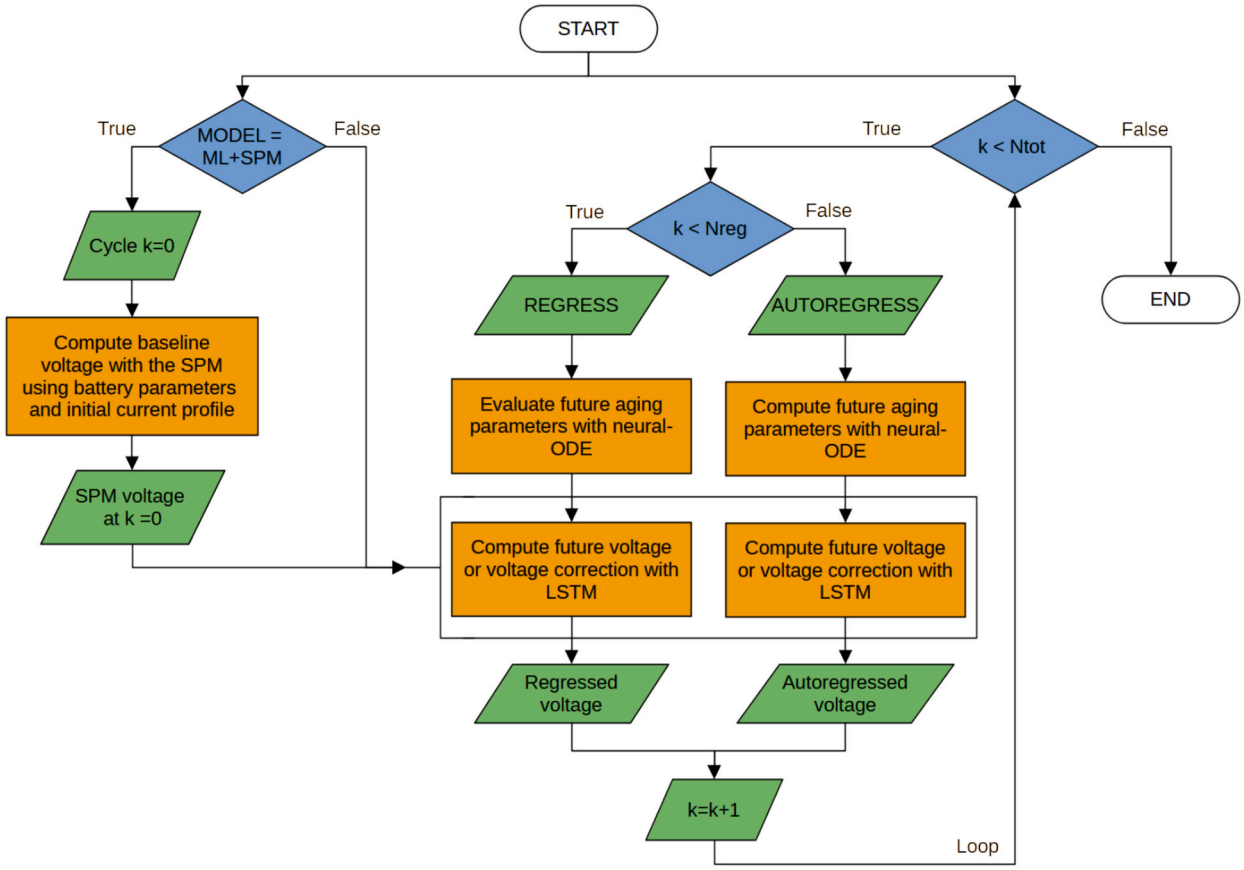

Fig. 2. Flowchart illustrating the structure of the ML and ML + SPM models. In the case of the ML + SPM model, the SPM model is used to compute the baseline voltage at the first cycle ($k = 0$) using the battery parameters and initial current. For each battery cycle, the neural-ODE and LSTM are then used to either regress or autoregress the voltage.

where N_{reg} is the number of points used to compare the trained ML and SPM-ML models, and $\widehat{V}_k$ and V_k are the regressed and experimental voltages at the cycle k for $k = 1, 2, \ldots, N_{reg}$, respectively. Furthermore, the RMSE from N_{reg} to N_{tot}, $RMSE_{autoreg}$, which was used for autoregressed segments, is given by

$$RMSE_{autoreg} = \sqrt{\frac{1}{N_{tot} - N_{reg}} \sum_{N_{reg}}^{N_{tot}} (\widehat{V}_k - V_k)^2} \quad (7)$$

where N_{tot} is the total number of cycle points. In addition to $RMSE_{reg}$ and $RMSE_{autoreg}$, the normalized voltage deviations were calculated using

$$\frac{\Delta V_k}{< V >} = \frac{\widehat{V}_k - V_k}{\frac{\sum_{k=1}^{N_{tot}} V_k}{N_{tot}}} \quad (8)$$

Last, the normalized $RMSE_{reg}$ and $RMSE_{autoreg}$ were derived by applying to Eq. (8) the mean square root over the cycle k.

3.3. Data preparation

Both experimental cycling datasets were used to compare the performance of both ML and ML + SPM models in mapping the current-voltage state space. First, the batteries were split into subgroups based on the manufacturer, as illustrated in Fig. 3(a).

Another subgroup of NMC batteries from the HKUST dataset was created and further subdivided depending on the discharge voltage cut-off, as shown in Fig. 3(b). 70 %, 10 %, and 20 % of the cycling data of the batteries in each subgroup were used for training, validation, and testing purposes, respectively. Finally, the models' regressive and autoregressive capabilities, where future values are predicted based on past data, were evaluated using the test data. The influence of the prediction window, *i.e.*, the number of cycles used for autoregression, was also investigated. To achieve this, the autoregressed voltage curves were compared against unseen data corresponding to 20 % and 80 % of the total number of cycles, N_{tot}. Importantly, N_{tot} was set to the lowest number of cycled data in each dataset, *i.e.*, $N_{tot} = 995$ and 44 for the HKUST and Oxford datasets, respectively. Furthermore, for the HKUST dataset, the cycle count was subsampled to 100 to expedite result convergence. Lastly, current and voltage curves were segmented into parts of 100 points through interpolation to maintain consistent input length for machine learning models. The learning rates of the neural-ODE and LSTM were initially tuned manually and then kept constant for all simulations, while the early-stopping criterion was used on the validation set to find the optimal number of iterations for each simulation.

4. Results

4.1. HKUST dataset

4.1.1. Analysis by battery type

First, the performance of the ML + SPM model was compared to that of the ML model using the batteries from the HKUST dataset for each manufacturer. For illustrative purposes, Fig. 4(a) shows the experimental voltages for a LISHEN cell for all cycles.

The voltages regressed with the SPM, ML, and ML + SPM models at the first cycle are displayed in Fig. 4(b). Graphically, the ML and ML + SPM models regressed the experimental voltage accurately. The close regression of the ML + SPM model stems from the correction term added to the voltage obtained with the SPM model, see Fig. 1. The voltage deviation obtained with the SPM, ML, and ML + SPM at the first and last cycles are shown for completeness in Fig. S1. Quantitatively, the values of $RMSE_{reg}$ and $RMSE_{autoreg}$ defined in Eqs. (6) and (7) are shown in Table 2. Except for the EVE cell, the values of both metrics were smaller for the ML + SPM model compared to those of the ML model. To allow comparison between different battery types, the normalized $RMSE_{reg}$ and $RMSE_{autoreg}$, defined in Section 3.2.1, are shown in Table S3. For the EVE battery, we observed discrepancies between SPM voltage predictions and experimental results (see Fig. S2(g)). This explains why the ML + SPM model, which incorporates SPM voltages, exhibited slightly lower accuracy in voltage regression and autoregression compared to the ML-only model. These results are detailed in Figs. 1 and 2, and Table 2. Next, the influence of the cycle number on the normalized voltage deviation, $\frac{\Delta V_k}{< V >}$ in Eq. (8), was evaluated. Fig. 4(c) shows the contour plot of these deviations obtained with the ML + SPM model using regression on 80 % of the total cycle number, and the last 20 % of the total cycle number for autoregression. Fig. 4(d) shows the contour plot obtained using the ML + SPM model with 20 % and 80 % of the total cycle number for regression and autoregression, respectively. In both cases, the deviations were not significantly affected when the cycle number was increased, demonstrating that aging was appropriately

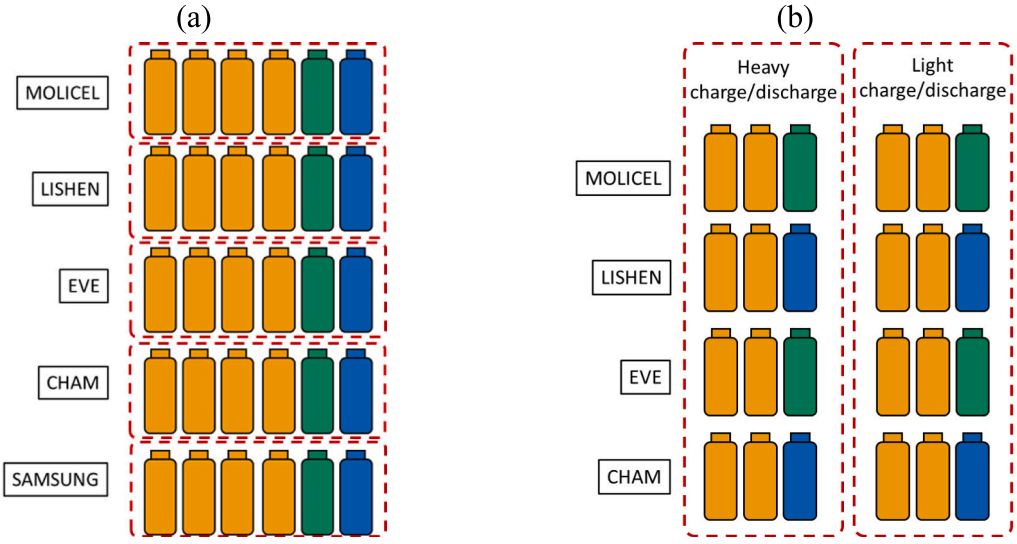

Fig. 3. Schematic representation of the HKUST batteries grouped by (a) cell manufacturer and (b) cathode chemistry and discharge protocol. The orange, green, and blue colors refer to the groups of batteries used for training, validation, and testing purposes, respectively. (For interpretation of the references to color in this figure legend, the reader is referred to the web version of this article.)

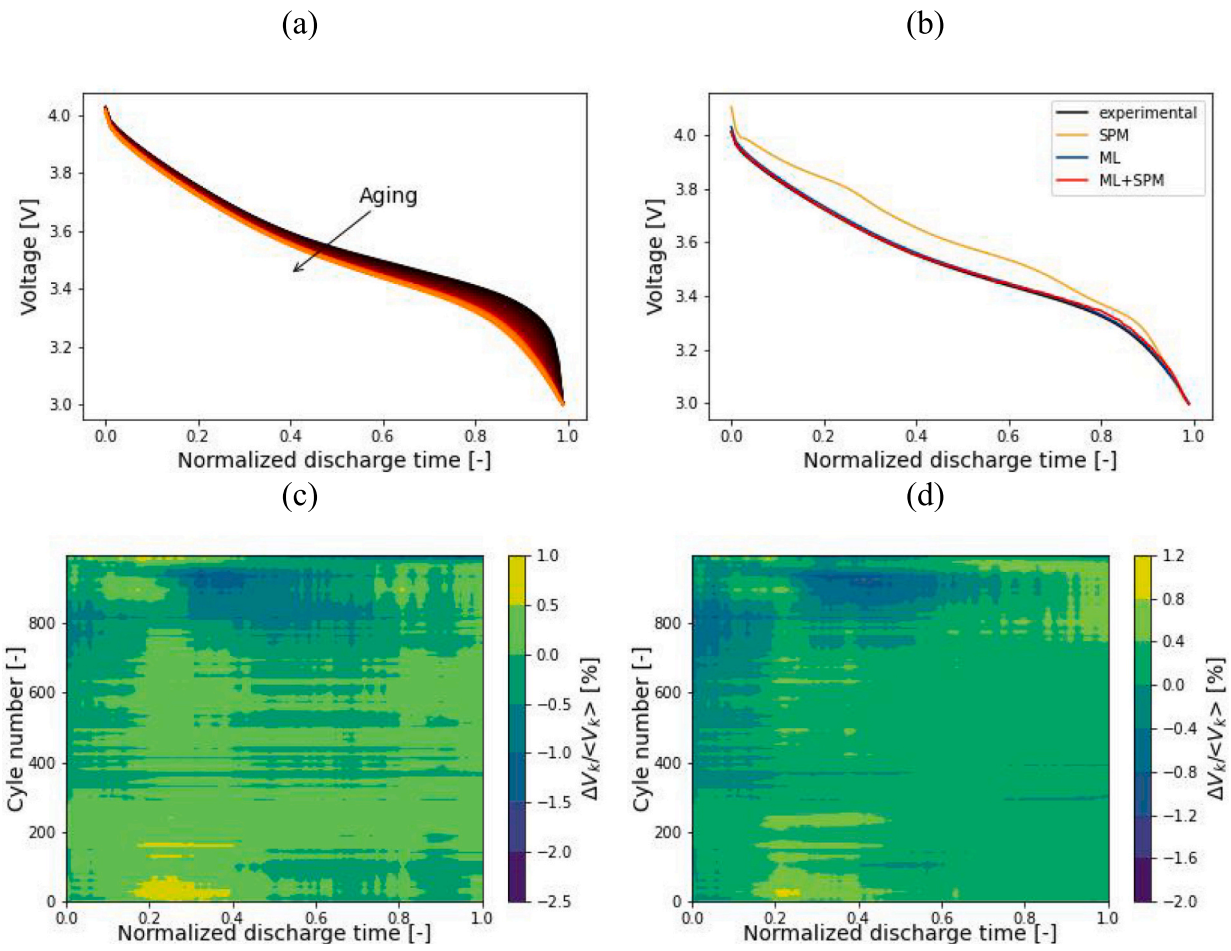

Fig. 4. For one LISHEN cell, (a) experimental voltages and (b) voltages regressed with the SPM, ML, and ML + SPM models with the experimental voltage also shown at the first cycle. The contour plots of the normalized voltage deviation as a function of the normalized discharge time and cycle number obtained using the ML + SPM model with regression and autoregression only on the last (c) 20 % and (d) 80 % of the total cycle number are also shown.

Table 2
For each battery manufacturer from the HKUST dataset, $RMSE_{reg}$ and $RMSE_{autoreg}$ values obtained with the ML and ML + SPM models. Best values are in bold.

Battery	ML		ML + SPM	
	$RMSE_{reg}$/mV	$RMSE_{autoreg}$/mV	$RMSE_{reg}$/mV	$RMSE_{autoreg}$/mV
MOLICEL	33.23	9.90	**12.27**	**5.95**
LISHEN	159.68	159.41	**15.67**	**25.32**
CHAM	100.35	102.06	**23.32**	**33.68**
EVE	**9.27**	**6.49**	17.66	13.93
SAMSUNG	100.35	102.06	**38.91**	**53.07**

accounted for by the ML + SPM model.

4.1.2. Analysis by charge/discharge protocol

To evaluate how the cycling protocol affects the performance of the ML and ML + SPM models, and how these two models handle clusters of batteries characterized by similar chemistries, all the NMC-type batteries from the HKUST dataset were used. This group was further subdivided into batteries which had undergone heavy and light cycling protocols. For each manufacturer and cycling protocol, Table 3 shows the values of $RMSE_{reg}$ and $RMSE_{autoreg}$ for the ML and ML + SPM models. Notably, grouping the batteries improved the performance of the ML model in 6 cases out of 8, see the values of $RMSE_{reg}$ and $RMSE_{autoreg}$ in Table 3, compared to the values in Table 2. One possible explanation lies in the fact that in the case where the cycling protocols were mixed

Table 3
For the EV29, CMF2, LSSA, and MLPA manufacturers, $RMSE_{reg}$ and $RMSE_{autoreg}$ values obtained with the ML and ML + SPM models. Best values are in bold.

Battery	ML		ML + SPM	
	$RMSE_{reg}$/mV	$RMSE_{autoreg}$/mV	$RMSE_{reg}$/mV	$RMSE_{autoreg}$/mV
Heavy charge/discharge				
MOLICEL	85.37	85.43	**35.97**	**34.40**
LISHEN	75.30	115.69	**70.00**	**76.69**
CHAM	132.83	82.26	**56.54**	**69.75**
EVE	**21.07**	24.09	34.49	**4.40**
Light charge/discharge				
MOLICEL	**22.24**	20.83	25.54	**20.57**
LISHEN	81.75	96.46	**64.60**	**47.07**
CHAM	**92.78**	**87.67**	112.65	116.71
EVE	**18.95**	22.53	27.76	**3.78**

during training and testing, the ML model was unable to accurately predict the voltage shape characteristic of each protocol (see Fig. S2). This issue was overcome using the ML + SPM model because the voltage from the SPM model was used as a baseline, which already accounted for modifications in the discharge-voltage profile due to the protocol. To overcome this issue for the ML model, the model parameters could be tuned to attribute more weight to features that encapsulate the protocol characteristics. To allow comparison between different battery types, the normalized $RMSE_{reg}$ and $RMSE_{autoreg}$ defined in Section 3.2.1 are presented in Table S4. Furthermore, compared with the heavy charge-

discharge protocol, the ML + SPM model did not consistently outperform the ML model under the light charge-discharge protocol. We attribute this behavior to the larger discrepancy between the SPM voltage predictions and experimental voltages in the light protocol compared to the heavy protocol (see Fig. S2).

4.2. Oxford dataset

The performance of the ML + SPM and ML models was further characterized using the Oxford dataset. Fig. 5(a) shows the experimental voltage trajectories of a given battery for all discharging cycles.

Characterization experiments took place every 100 cycles, reflecting the snapshot presented in Fig. 5(a). The actual and projected voltages at the battery's initial cycle are shown in Fig. 5(b), with predictions derived from the ML and ML + SPM models. For comparison purposes, the voltage deviations obtained with the SPM, ML, and ML + SPM models at the first and last cycles are shown in Fig. S1. Overall, both the ML and ML + SPM models replicated the experimental voltages with exceptional precision. The mean $RMSE_{reg}$ is equal to 0.28 % and 0.11 % for the ML and ML + SPM, respectively, while the corresponding mean $RMSE_{autoreg}$ is equal to 2.68 % and 0.67 %. The contour plots of the normalized voltage deviations (see Eq. (8)) are shown in panels (c) and (d) of Fig. 5. Specifically, Fig. 5(c) and (d) displays the results when autoregression is applied to the last 20 % and 80 % of the total cycle numbers, respectively. Voltage prediction appears less accurate towards the last cycles and at extreme normalized discharge times (<0.2 and > 0.8). This is confirmed in Fig. 5(d), which exhibits higher voltage discrepancies when compared to Fig. 5(c).

4.3. Influence of the prediction window

Next, the influence of the prediction window on the models for all batteries was investigated using autoregression on the last 20 % or 80 % of N_{tot}. Fig. 6(a) shows the $RMSE_{autoreg}$ obtained with the SPM (yellow), ML (blue), and ML + SPM (red) models for both autoregression windows (light and dark colors are used to distinguish the 20 % and 80 % autoregression windows, respectively). In all scenarios, except for the EVE batteries, the ML model's accuracy diminishes for longer autoregression windows (*i.e.*, in the 80 % window scenario represented in dark blue). For the EVE batteries, we note that the RMSE for autoregression for the 20 % window scenario is comparable and slightly higher than that for the 80 % scenario. The ML + SPM model (red bars) consistently outperformed both the SPM (yellow bars) and ML (blue bars) models for autoregressed windows across all batteries except the EVE cells (a possible explanation is provided in Section 4.1.1). The ML model's lower performance with LISHEN, CHAM, and SAMSUNG batteries is likely due to its inability to independently identify the unique shape of the voltage profile based solely on input currents. This limitation leads to decreased accuracy when the ML model is trained and tested on diverse cycling protocols. A more detailed analysis is presented in Fig. 6, where panels (b) and (c) depict the normalized voltage ($\frac{\Delta V_k}{<V>}$, see Eq. (8)) over discharge time and cycle life, respectively, for one of the LISHEN cells using the ML model under 20 % and 80 % window. A slight degradation in prediction performance is observed towards the end of life with larger autoregression windows (panel (c)). Panels (d) and (e) of Fig. 6 illustrate the same metrics for the ML + SPM model under 20 % and 80 % window scenarios, respectively. Notably, the discrepancy between the prediction

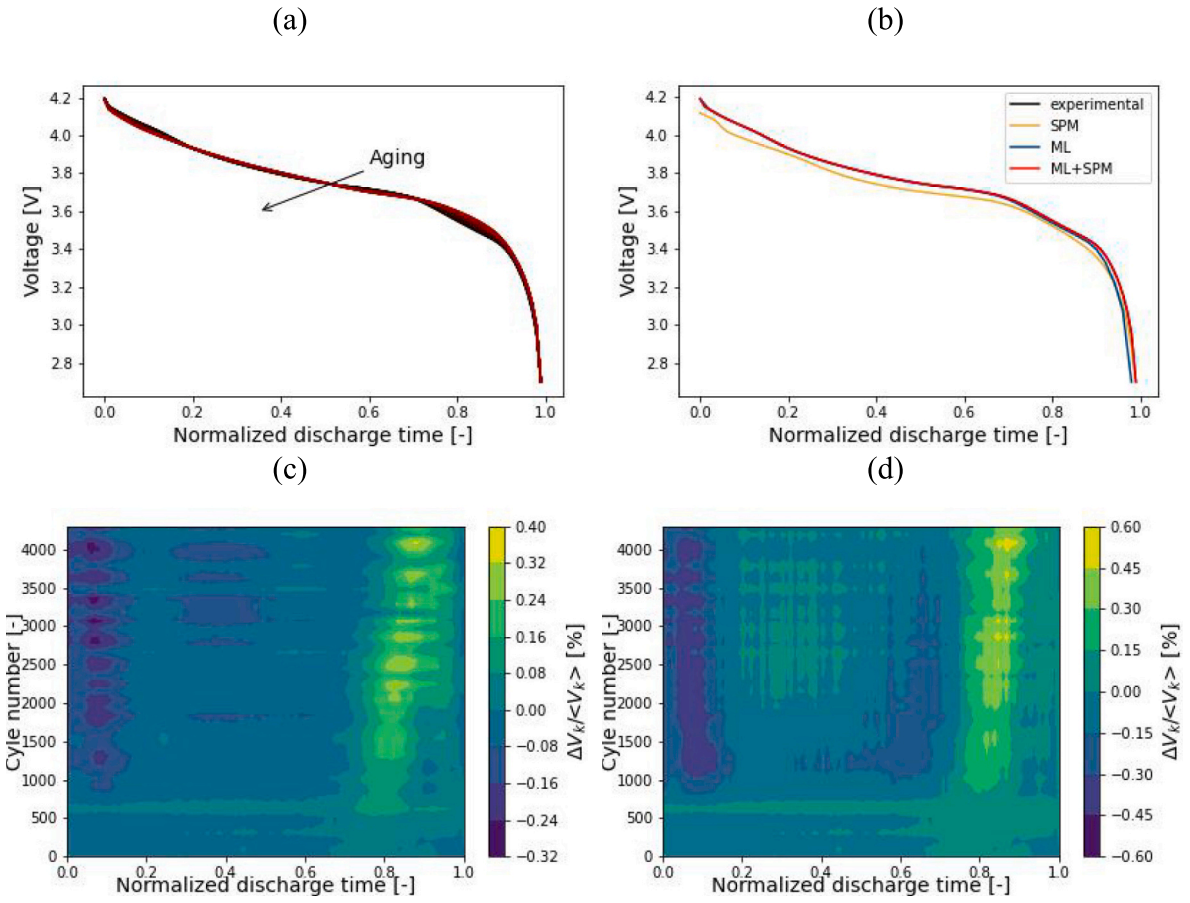

Fig. 5. For one Oxford cell, (a) experimental voltages and (b) voltages regressed with the SPM, ML, and ML + SPM models with the experimental voltages also shown at the first cycle. The contour plots of the normalized voltage deviation as a function of the normalized discharge time and cycle number obtained using the ML + SPM model with regression and autoregression only on the last (c) 20 % and (d) 80 % of the total cycle number are also shown.

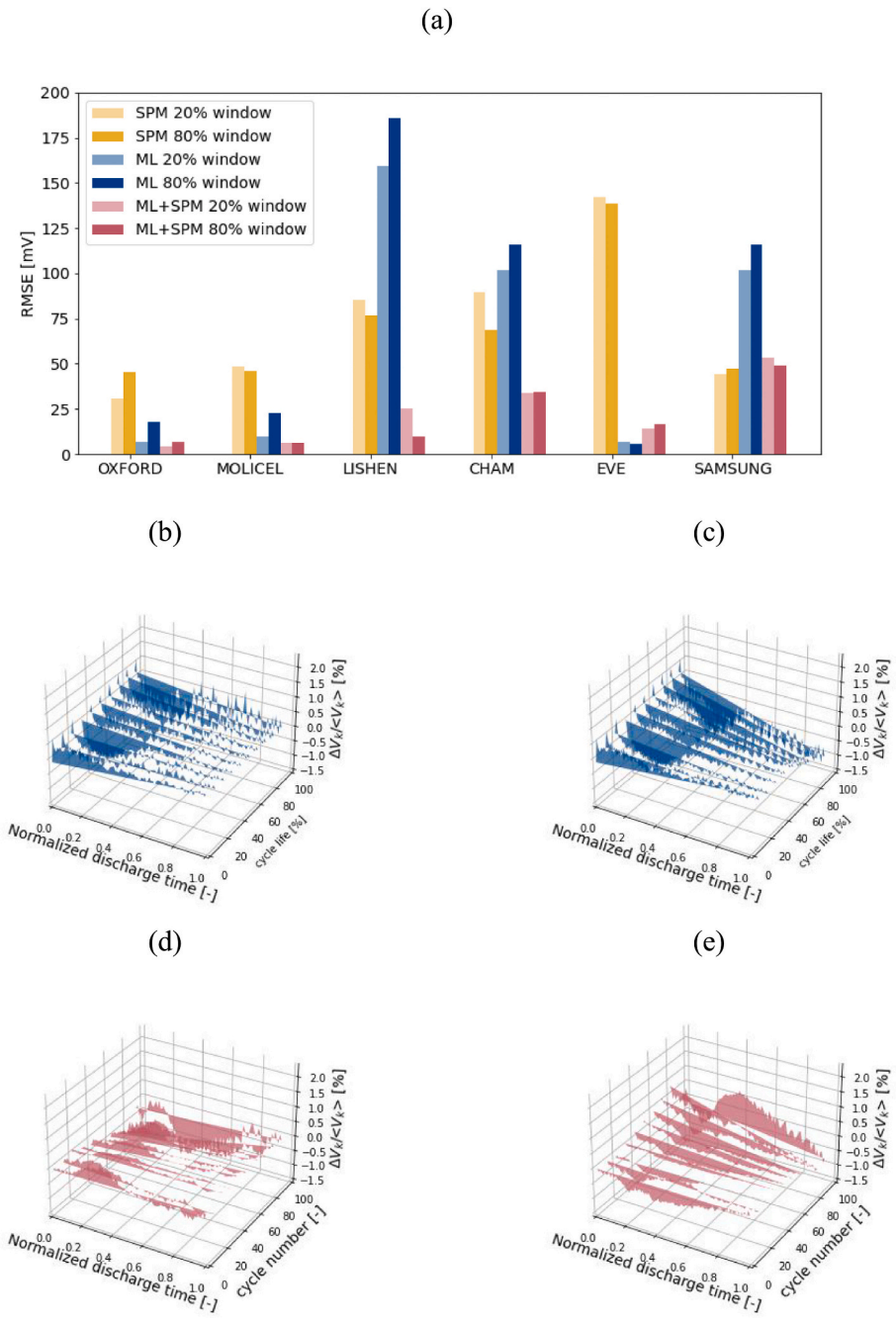

Fig. 6. (a) $RMSE_{autoreg}$ values obtained using the SPM, ML, and ML + SPM models for the Oxford dataset and each manufacturer of the HKUST batteries. For a LISHEN battery, the normalized voltage deviations obtained with the ML model and an autoregression window of (b) 20 % and (c) 80 % are also shown. The corresponding plots for the ML + SPM model are displayed in panels (d) and (e).

modalities is less pronounced in these cases compared to those obtained with the ML model alone (panels (b) and (c)), except for the final cycles. Importantly, this new hybrid model also outperforms the standalone SPM and ML models when predicting battery voltages under various experimental conditions. As outlined in the introduction (Section 1) and conclusion (Section 5), this improvement stems from the ML + SPM model's ability to combine the advantages of each individual model. Specifically, the SPM model incorporates the physics principles missing in ML models, while the latter are more flexible and adaptable than the SPM model.

5. Conclusions

In this work, two established approaches for analyzing the voltage and aging states of batteries were combined, namely physical and ML-based models. We proposed a new hybrid model that integrates a single particle model with both a neural-ODE and an LSTM neural network. Using a new cycling dataset collected by our group, encompassing a broad range of battery voltages, chemistries, and capacities, the hybrid ML + SPM model was shown to be more accurate than the individual ML models in most cases. This result was further confirmed using the Oxford dataset. Additionally, the hybrid model demonstrated improved performance with longer prediction windows compared to the SPM and ML models in isolation.

While the precise mechanisms underlying its superior performance should be further investigated, the ML + SPM model likely derives its advantages from a combination of the adaptability inherent in the ML model and the physical insights offered by the SPM model. This synergy enables the model to accurately predict future states by initializing voltage profiles based on the SPM model and subsequently refining them with the ML model, thereby optimizing the forecasting process. Future work should further elucidate these mechanisms by examining the influence of varying cycling temperatures on model performance, as well as the degradation at a downsampled frequency of cycle numbers. Another promising avenue of research is the analysis of large datasets to address practical situations, such as battery management systems in electric vehicles.

This work establishes a foundation for the development of next-generation physics-supported battery models, characterized by reduced computational demands suitable for integration into battery management systems. Our findings underscore the value of machine learning techniques, particularly when knowledge of underlying physicochemical mechanisms is limited. However, the incorporation of fundamental physical principles remains essential for maintaining high predictive accuracy and reliability. The proposed approach facilitates real-time battery state estimation, diagnosis, and future state prediction, enabling continuous monitoring of voltage responses to 26 applied currents. This capability is crucial for mitigating safety risks associated with battery operation, including malfunction prediction and state-of-health assessment.

List of symbols

$\mathbf{AP}_k$	Aging parameters at the k-th cycle
N_{reg}	Number of points used for regression
N_{tot}	Maximum number of cycles
$\text{RMSE}_{\text{autoreg}}$	Root mean square for the autoregression
RMSE_{reg}	Root mean square for the regression
SOH_k	State of health at the k-th cycle
$t_{\text{C},k}$	Total charging time at constant current at the k-th cycle
$t_{\text{DC},k}$	Total discharging time at constant current at the k-th cycle
V_k	Experimental voltage at the k-th cycle
$\widehat{V}_k$	Modeled voltage at the k-th cycle
$\frac{\Delta V_k}{< V >}$	Normalized voltage deviations at the k-th cycle

List of abbreviations

LSTM	Long-short-term memory
ML	Machine learning
NCA	Nickel cobalt aluminum
NMC	Nickel manganese cobalt
ODE	Ordinary differential equation
PyBAMM	Python battery mathematical modelling
RMSE	Root mean square error
SOH	State of health
SPM	Single particle model

CRediT authorship contribution statement

Simona Pepe: Writing – review & editing, Writing – original draft, Visualization, Software, Formal analysis, Data curation, Conceptualization. **Lok Shu Kwan:** Data curation. **Baptiste Py:** Writing – review & editing, Visualization, Methodology. **Matthew J. Robson:** Writing – review & editing, Software, Methodology. **Adeleke Maradesa:** Writing – review & editing, Visualization. **Francesco Ciucci:** Writing – review & editing, Methodology, Funding acquisition, Formal analysis.

Declaration of Generative AI and AI-assisted technologies in the writing process

During the preparation of this work the authors used Generative Pre-trained Transformer in order to improve the readability and language. After using this tool, the authors reviewed and edited the content as needed and take full responsibility for the content of the publication.

Declaration of competing interest

None.

Acknowledgments

The authors gratefully acknowledge the financial support from the Research Grants Council of Hong Kong (RGC Ref No. 18201820 and 16201622). This work was supported in part by the University of Bayreuth and the Bavarian Center for Battery Technology (BayBatt) through start-up funding. Lastly, S. Pepe, B. Py, M.J. Robson, and A. Maradesa kindly thank the Hong Kong PhD. Fellowship Scheme for its financial support.

Appendix A. Supplementary data

Supplementary data to this article can be found online at https://doi.org/10.1016/j.est.2024.115044.

Data availability

Data are available at https://github.com/simonapepe/HKUST-dataset.git.

References

[1] A.G. Olabi, M.A. Abdelkareem, Renewable energy and climate change, Renew. Sust. Energ. Rev. 158 (2022) 112111.
[2] H. Chen, T.N. Cong, W. Yang, C. Tan, Y. Li, Y. Ding, Progress in electrical energy storage system: a critical review, Progress, Nat. Sci. 19 (2009) 291–312.
[3] G. Zubi, R. Dufo-López, M. Carvalho, G. Pasaoglu, The lithium-ion battery: state of the art and future perspectives, Renew. Sust. Energ. Rev. 89 (2018) 292–308.
[4] Y. Wang, J. Tian, Z. Sun, L. Wang, R. Xu, M. Li, Z. Chen, A comprehensive review of battery modeling and state estimation approaches for advanced battery management systems, Renew. Sust. Energ. Rev. 131 (2020) 110015.
[5] C.D. Rahn, C.Y. Wang, Battery System Engineering, John Wiley & Sons, 2013.
[6] M. Doyle, T.F. Fuller, J. Newman, Modeling of galvanostatic charge and discharge of the lithium/polymer/insertion cell, J. Electrochem. Soc. 140 (1993) 1526–1533.
[7] V. Sulzer, S.G. Marquis, R. Timms, M. Robinson, S.J. Chapman, Python battery mathematical modelling (PyBaMM), J. Open Research Software. 9 (2021).
[8] S.J. Moura, F.B. Argomedo, R. Klein, A. Mirtabatabaei, M. Krstic, Battery state estimation for a single particle model with electrolyte dynamics, IEEE Trans. Contr. Syst. Technol. 25 (2017) 453–468.
[9] S. Santhanagopalan, Q. Guo, P. Ramadass, R.E. White, Review of models for predicting the cycling performance of lithium ion batteries, J. Power Sources 156 (2006) 620–628.
[10] X. Han, M. Ouyang, L. Lu, J. Li, Simplification of physics-based electrochemical model for lithium ion battery on electric vehicle. Part I: diffusion simplification and single particle model, J. Power Sources 278 (2015) 802–813.
[11] S.J. Moura, M. Krstic, N.A. Chaturvedi, Adaptive PDE observer for battery SOC/SOH estimation, in: Dynamic Syst. Control Conf, 2022, pp. 101–110.
[12] A.G. Li, A.C. West, M. Preindl, Towards unified machine learning characterization of lithium-ion battery degradation across multiple levels: a critical review, Appl. Energy 316 (2022) 119030.
[13] J.F. Whitacre, J. Mitchell, A. Dave, W. Wu, S. Burke, V. Viswanathan, An autonomous electrochemical test stand for machine learning informed electrolyte optimization, J. Electrochem. Soc. 166 (2019) A4181–A4187.
[14] A. Weng, P. Mohtat, P.M. Attia, V. Sulzer, S. Lee, G. Less, A. Stefanopoulou, Predicting the impact of formation protocols on battery lifetime immediately after manufacturing, Joule 5 (2021) 2971–2992.
[15] P.M. Attia, A. Grover, N. Jin, K.A. Severson, T.M. Markov, Y.H. Liao, M.H. Chen, B. Cheong, N. Perkins, Z. Yang, Closed-loop optimization of fast-charging protocols for batteries with machine learning, Nature 578 (2020) 397–402.
[16] X. Hu, L. Xu, X. Lin, M. Pecht, Battery lifetime prognostics, Joule 4 (2020) 310–346.
[17] R. Refai, S. Yayathi, D. Chen, B. Fernandez-Rodriguez, Hybrid neural net model of a lithium ion battery, Dynamic Syst, Control Conf. (2011) 239–246.

[18] H. Tu, S. Moura, Y. Wang, H. Fang, Integrating physics-based modeling with machine learning for lithium-ion batteries, Appl. Energy 329 (2023) 120289.
[19] S. Park, D. Zhang, S. Moura, Hybrid electrochemical modeling with recurrent neural networks for Li-ion batteries, 2017 American Control Conf. (2017) 3777–3782.
[20] F. Feng, S. Teng, K. Liu, J. Xie, Y. Xie, B. Liu, K. Li, Co-estimation of lithium-ion battery state of charge and state of temperature based on a hybrid electrochemical-thermal-neural-network model, J. Power Sources 455 (2020) 227935.
[21] R.T. Chen, Y. Rubanova, J. Bettencourt, D. Duvenaud, Neural ordinary differential equations, arXiv Preprint arXiv:1806.07366 (2018).
[22] S. Hochreiter, J. Schmidhuber, LSTM can solve hard long time lag problems, Adv. Neural Inf. Proces. Syst. 9 (1996) 473–479.
[23] S. Pepe, J. Liu, E. Quattrocchi, F. Ciucci, Neural ordinary differential equations and recurrent neural networks for predicting the state of health of batteries, J. Energy Storage. 50 (2022) 104209.
[24] F.A. Gers, J. Schmidhuber, F. Cummins, Learning to forget: continual prediction with LSTM, Neural Comput. 12 (2000) 2451–2471.
[25] C. Birkl, Oxford Battery Degradation Datset, 2017, p. 1.
[26] R.R. Richardson, M.A. Osborne, D.A. Howey, Gaussian process regression for forecasting battery state of health, J. Power Sources 357 (2017) 209–219.
[27] S.G. Marquis, V. Sulzer, R. Timms, C.P. Please, S.J. Chapman, An asymptotic derivation of a single particle model with electrolyte, J. Electrochem. Soc. 166 (2019) A3693–A3706.
[28] C.H. Chen, F. Brosa Planella, K. O'Regan, D. Gastol, W.D. Widanage, E. Kendrick, Development of experimental techniques for parameterization of multi-scale lithium-ion battery models, J. Electrochem. Soc. 167 (2020) 080534.
[29] G.H. Kim, K. Smith, K.J. Lee, S. Santhanagopalan, A. Pesaran, Multi-domain modeling of lithium-ion batteries encompassing multi-physics in varied length scales, J. Electrochem. Soc. 158 (2011) A955.
[30] Y. Zhao, Y. Patel, T. Zhang, G.J. Offer, Modeling the effects of thermal gradients induced by tab and surface cooling on lithium ion cell performance, J. Electrochem. Soc. 165 (2018) A3169–A3178.
[31] G. Richardson, I. Korotkin, R. Ranom, M. Castle, J.M. Foster, Generalised single particle models for high-rate operation of graded lithium-ion electrodes: systematic derivation and validation, Electrochim. Acta 339 (2020) 135862.
[32] A. Hales, L.B. Diaz, M.W. Marzook, Y. Zhao, Y. Patel, G. Offer, The cell cooling coefficient: a standard to define heat rejection from lithium-ion batteries, J. Electrochem. Soc. 166 (2019) A2383–A2395.
[33] M. Ecker, T.K.D. Tran, P. Dechent, S. Käbitz, A. Warnecke, D.U. Sauer, Parameterization of a physico-chemical model of a lithium-ion battery: I. Determination of parameters, J. Electrochem. Soc. 162 (2015) A1836–A1848.
[34] M. Ecker, S. Käbitz, I. Laresgoiti, D.U. Sauer, Parameterization of a physico-chemical model of a lithium-ion battery: II. Model validation, J. Electrochem. Soc. 162 (2015) A1849–A1857.
[35] R.T. Chen, Y. Rubanova, J. Bettencourt, D.K. Duvenaud, Neural ordinary differential equations, Adv. Neural Inf. Proces. Syst. 31 (2018).
[36] X. Hu, Y. Che, X. Lin, S. Onori, Battery health prediction using fusion-based feature selection and machine learning, IEEE Trans. Transp. Electrif. 7 (2021) 382–398.
[37] Q. Zhang, L. Yang, W. Guo, J. Qiang, C. Peng, Q. Li, Z. Deng, A deep learning method for lithium-ion battery remaining useful life prediction based on sparse segment data via cloud computing system, Energy 241 (2022) 122716.